Hydrothermal fluids and where to find them: Using seismic attenuation and anisotropy to map fluids beneath Uturuncu volcano, Bolivia

Thomas Samuel Hudson[1], John-Michael Kendall[1], Jon D Blundy[2], Matthew E Pritchard[3], Patricia MacQueen[3], Shawn Wei[4], Joachim Gottsmann[5], and Sacha Lapins[5]

[1]University of Oxford
[2]Oxford University
[3]Cornell University
[4]Michigan State University
[5]University of Bristol

November 22, 2022

Abstract

Mapping fluid accumulation in the crust is pertinent for numerous applications including volcanic hazard assessment, geothermal energy generation and mineral exploration. Here, we use seismic attenuation tomography to map the distribution of fluids in the crust below Uturuncu volcano, Bolivia. Seismic P-wave and S-wave attenuation, as well as their ratio (Q_P/Q_S), constrain where the crust is partially and fully fluid-saturated. Seismic anisotropy observations further constrain the mechanism by which the fluids accumulate, predominantly along aligned faults and fractures in this case. Furthermore, subsurface pressure-temperature profiles and conductivity data allow us to identify the most likely fluid composition. We identify shallow regions of both dry and H_2O/brine-saturated crust, as well as a deeper supercritical H_2O/brine column directly beneath Uturuncu. Our observations provide a greater understanding of Uturuncu's transcrustal hydrothermal system, and act as an example of how such methods could be applied to map crustal fluid pathways and hydrothermal/geothermal systems elsewhere.

Hydrothermal fluids and where to find them: Using seismic attenuation and anisotropy to map fluids beneath Uturuncu volcano, Bolivia

T.S. Hudson[1], JM. Kendall[1], J.D. Blundy[1], M.E. Pritchard[2], P. MacQueen[2], S.S. Wei[3], J.H. Gottsmann[4], S. Lapins[4]

[1]Department of Earth Sciences, University of Oxford, UK
[2]Department of Earth and Atmospheric Sciences, Cornell University, USA
[3]Department of Earth and Environmental Sciences, Michigan State University, USA
[4]School of Earth Sciences, University of Bristol, UK

Corresponding author: Thomas S. Hudson (thomas.hudson@earth.ox.ac.uk)

Key Points:

- Seismic attenuation tomography can map crustal fluids and elucidate whether fluids are compressible, incompressible or supercritical
- S-wave velocity anisotropy suggests that crustal fluids at Uturuncu migrate and/or accumulate along fractures
- Seismic attenuation combined with temperature, pressure and conductivity measurements can provide constraint on fluid composition

Abstract

Mapping fluid accumulation in the crust is pertinent for numerous applications including volcanic hazard assessment, geothermal energy generation and mineral exploration. Here, we use seismic attenuation tomography to map the distribution of fluids in the crust below Uturuncu volcano, Bolivia. Seismic P-wave and S-wave attenuation, as well as their ratio (Q_P/Q_S), constrain where the crust is partially and fully fluid-saturated. Seismic anisotropy observations further constrain the mechanism by which the fluids accumulate, predominantly along aligned faults and fractures in this case. Furthermore, subsurface pressure-temperature profiles and conductivity data allow us to identify the most likely fluid composition. We identify shallow regions of both dry and H_2O/brine-saturated crust, as well as a deeper supercritical H_2O/brine column directly beneath Uturuncu. Our observations provide a greater understanding of Uturuncu's transcrustal hydrothermal system, and act as an example of how such methods could be applied to map crustal fluid pathways and hydrothermal/geothermal systems elsewhere.

Plain Language Summary

Locating where water/brines, gas and molten rock are in the crust is important various applications, including assessing volcanic hazard, generating geothermal energy and exploring for critical metals. Here, we map how seismic energy is absorbed (or attenuated) in Earth's crust, in order to look for fluids in the subsurface. We do this at Uturuncu volcano, Bolivia. This allows us to image whether the crust is partly or fully saturated with fluids. We also use seismic anisotropy to help us understand how the seismic energy is absorbed. We then use other data, including pressure, temperature and electrical conductivity data to identify what fluids can be found where. We find that we can map where water/brines are and whether they contain carbon dioxide (i.e. are "sparkling") or not (i.e. "still").

1 Introduction

Fluids are present in much of Earth's crust. Mapping where and why these fluids accumulate, as well as identifying their composition are critical questions in the earth sciences. For example, understanding where magma resides is important for volcanic hazard assessment, mapping the extent of geothermal systems is pertinent for maximising production efficiency, and identifying the location and properties of metal-rich brines is relevant for mineral exploration. The question that this study addresses is: can seismic attenuation combined with seismic anisotropy be used to map the location of fluids and, in combination with auxiliary data, identify fluid composition? Here, we test this hypothesis at Uturuncu volcano, Bolivia.

Uturuncu volcano sits within the Bolivian Andes. The volcano last erupted 250,000 yrs ago (Muir et al., 2015), yet has exhibited significant uplift at rates of up to 1 cm/yr (Gottsmann et al., 2018; Pritchard et al., 2018). Uturuncu lies ~20 km above the Altiplano-Puna Magma (or Mush) Body (APMB), Earth's largest body of silicic partial melt (Pritchard et al., 2018). This melt heats the crust above and potentially provides a source of ascending metal-rich volatiles (Blundy et al., 2021). Uturuncu provides an ideal location for attempting to image and identify fluids, since the host crust isolated from the volcanic system is likely predominantly unsaturated except near surface rivers/lakes, while a shallow, partially-saturated hydrothermal system likely exists under the volcano that is sustained via heat and volatiles from the APMB (Gottsmann et al., 2022).

Here, we use microseismicity at Uturuncu (Hudson et al., 2022) to perform seismic attenuation tomography and anisotropy analysis. Seismic attenuation is sensitive to the presence of fluids, with tomography enabling any fluids to be mapped (e.g. Hauksson & Shearer, 2006). Attenuation studies of volcanoes have previously been undertaken (Bohm et al., 2013; Caudron et al., 2019; Gudmundsson et al., 2004; Lanza et al., 2020; Lees, 2007; O'Brien & Bean, 2009; Sanders et al., 1995; De Siena et al., 2014; Zhao, 2001). Seismic anisotropy in volcanic or tectonic regions is predominantly sensitive to fault structures (e.g. Baird et al., 2015), enabling one to identify whether fluids migrate and accumulate along volcanic and/or fault structures (Bacon et al., 2021; Baird et al., 2015; Gerst & Savage, 2004; Johnson et al., 2011; Maher & Kendall, 2018; Nowacki et al., 2018). The novelty of this work lies in using seismic attenuation and anisotropy to identify the dominant attenuation mechanism and fluid saturation level. We then combine these results with auxiliary pressure, temperature and electrical conductivity profiles (Comeau et al., 2016; Pritchard et al., 2018), to infer fluid composition and ascertain how fluids migrate and accumulate in the crust.

2 Methods

2.1 Earthquake catalogue

The Uturuncu earthquake catalogue used in this study is from Hudson et al. (2022). Seismicity is detected using the PLUTONS network (Kukarina et al., 2017), which was deployed from the 13th April 2010 to the 27th October 2012. The PLUTONS network comprised of thirty-three Guralp CMG-3T *120 s* seismometers recording at 100 Hz. Earthquakes are detected using QuakeMigrate (Hudson et al., 2019; Smith et al., 2020) and relocated using NonLinLoc (Lomax & Virieux, 2000).

The velocity model is the same as in Hudson et al. (2022). This produces a catalogue of 1356 earthquakes, which we use in this study (see Supplementary Figure 1).

2.2 Seismic attenuation

Seismic attenuation is the loss of energy of a seismic wave into the medium during propagation. The amplitude of a seismic wave, $A(\boldsymbol{x}, f)$, at a position $\boldsymbol{x}$ with a frequency f, is defined by (Aki & Richards, 2002),

$$A(\boldsymbol{x}, f) = A_0(\theta, \phi) G(\boldsymbol{x}) e^{-\alpha(f) r(x)} \quad ,$$

where $A_0(\theta, \phi)$ is the source amplitude in the direction θ from vertical and ϕ from North, $G(\boldsymbol{x})$ is a geometrical spreading factor, $r(\boldsymbol{x})$ is the ray path length, and $\alpha(f)$ is the attenuation factor for a particular frequency. Therefore, the greater the value of α, the greater the attenuation.

In seismology, the convention is to quantify attenuation using the seismic quality factor, Q, the inverse of α, which is given by (Aki & Richards, 2002),

$$Q_i = \frac{\pi f}{v_i \, \alpha(f)} \quad ,$$

where v_i is the velocity of phase i (P or S). Here, we approximate α, and therefore Q, to be frequency-independent over the bandwidth of the earthquakes studied ($0.5 \ to \ 20 \ Hz$).

2.2.1 Attenuation tomography

Attenuation tomography uses path-averaged attenuation observations, Q_{path}, between earthquake sources and receivers, to map the attenuation structure. The 3D attenuation tomography performed in this study uses the earthquakes and receivers shown in Supplementary Figure 1, with the ray paths shown in Supplementary Figure S2 and S3. Our method is based upon that described in Wei & Wiens (2018), with some alterations due to the local nature of our study area. A full description of the attenuation tomography methodology can be found in the Supplementary Information.

2.2.2 Q_P/Q_S ratios

P-wave attenuation is sensitive to scattering from faults and other velocity contrasts, as well as the intrinsic attenuation of the host rock and other compressible media, such as supercritical fluids and gases. S-wave attenuation is also sensitive to the scattering from fault structures and the presence of fluids, but in contrast to P-waves is insensitive to the compressibility of fluids (Chapman, 2003; Chapman et al., 2021; Klimentos, 1995). Attenuation tomography therefore not only allows for mapping the presence of any fluids, but Q_P/Q_S ratios are also diagnostic of fluid saturation, with $Q_P/Q_S < 1$ indicating that rock is only partially-saturated and $Q_P/Q_S > 1$ suggesting fully-saturated rock (Amalokwu et al., 2014; Hauksson & Shearer, 2006; K. Winkler & Nur, 1979). Here, we assume the concept of partially-saturated rock in its broadest sense, in that it simply has to have some fraction of compressible fluid or gas present (see Figure 4).

2.3 Seismic anisotropy

Seismic anisotropy in this study refers to S-wave velocity anisotropy, measured from shear-wave splitting. Such anisotropy can be broadly attributed to two factors: crystallographic preferred orientation, where individual crystals of the medium preferentially align; and shape-preferred orientation anisotropy, typically caused by the preferential alignment of fractures (Kendall, 2000). As an S-wave propagates through an anisotropic region, the energy will be partitioned into two orthogonal components, one oriented in the plane of the fast-direction, ϕ, and the other in the plane of the slow-direction. This phenomenon is called shear-wave splitting (Crampin, 1981; Silver & Chan, 1991), measured here using SWSPy (Hudson, 2022). ϕ is controlled by the orientation of the fabric and/or fractures. The arrival-time difference between the fast and slow S waves, δt, is controlled by the strength and/or spatial extent of the anisotropy.

3 Results

The overall attenuation tomography results for Q_P, Q_S and Q_P/Q_S are shown in Figure 1. Tomographic resolution test results, based on the point-spread-function method (Rawlinson & Spakman, 2016), are shown in Supplementary Figure S2 and S3. Regional Q_P values are ~200-300, while regional Q_S values range from 200-400. These values fall within the range observed at similar crustal depths elsewhere (Hauksson & Shearer, 2006; Lanza et al., 2020; Del Pezzo et al., 1995). Regional Q_P and Q_S both generally increase with depth, as expected for denser crust. A region of lower Q_P (high attenuation) extends in the SE-NW direction, intersecting Uturuncu. This high attenuation region extends to depths of 8 km bsl. Q_S follows the SE-NW trend observed in Q_P, except with more isolated pockets of lower Q_S (high attenuation) rather than a continuous band. These isolated pockets occur on lateral length scales of ~5-10 km and extend to depths of up to 3 km bsl. One exception is a highly attenuating region ~ 15 km North of Uturuncu, at a depth of ~12 km bsl. However, it should be noted that this feature is at the limit of the resolvable region (see Supplementary Figure S2 and S3).

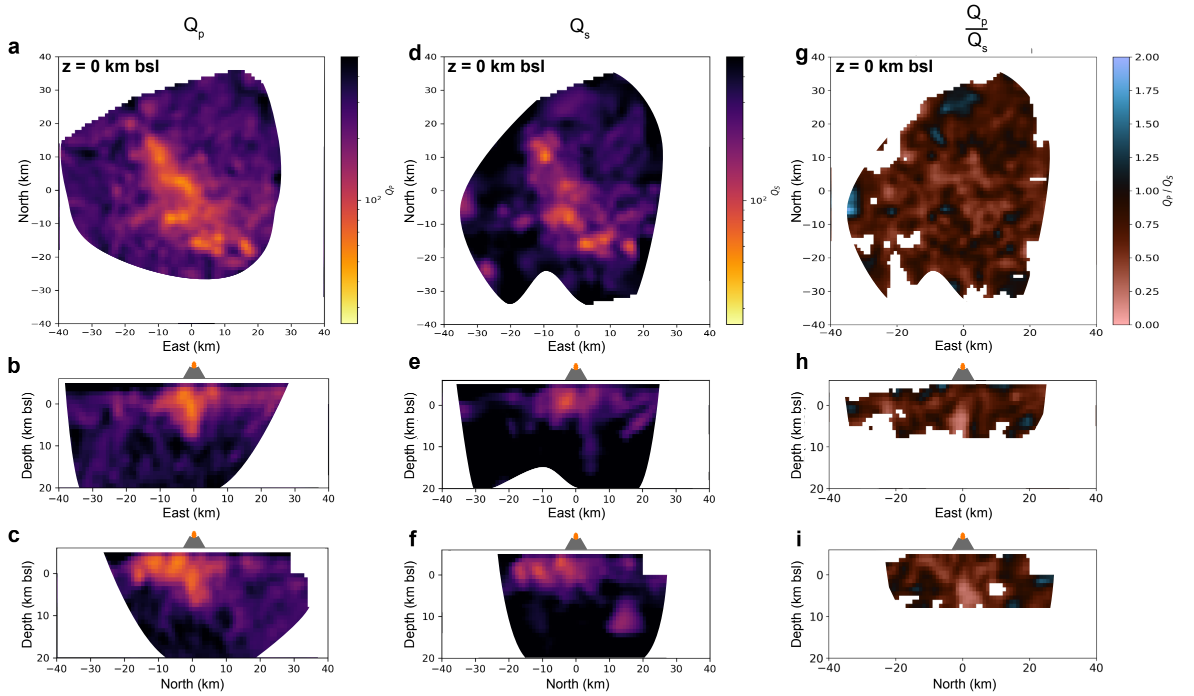

Figure 1*. Overall attenuation tomography results for an 80x80 km region surrounding Uturuncu volcano, Bolivia. (a) to (c): Map, WE and SN profiles, respectively, for Q_P. (d) to (f): Map, WE and SN profiles, respectively, for Q_S. (g) to (i): Map, WE and SN profiles, respectively, for Q_P/Q_S. Uturuncu is located at 0 km N, 0 km E. Map profiles are for 0 km bsl, and depth*

profiles are for 0 km N and 0 km E of Uturuncu, respectively. Masked areas correspond to regions where features of at least 4 km size cannot be resolved (see Supplementary Figures 1 and 2 for resolution tests). Additionally, Q_P/Q_S results masked where Q_P and/or Q_S > 500 (see Discussion for justification on masks).

The majority of the region has $Q_P/Q_S < 1$ (see Figure 1g-i). A significant feature is a column of $Q_P/Q_S \ll 1$ directly beneath Uturuncu's summit, extending from 1-2 km bsl to at least 8 km bsl. This feature is shown in greater detail in Figure 2a-c (labelled A), where Q_P/Q_S is compared to resistivity tomography results from Comeau et al. (2016). Feature A corresponds to a region of low resistivity (< 10 Ω m), indicative of high-salinity brines (Afanasyev et al., 2018). Isolated features with $Q_P/Q_S > 1$ also exist. One such feature, beneath Cerro Loromayo (Fracchia, 2009; Soler et al., 2007), is shown in detail in Figure 2d-f (labelled C). This feature also corresponds to a region of low resistivity, as do other $Q_P/Q_S > 1$ regions.

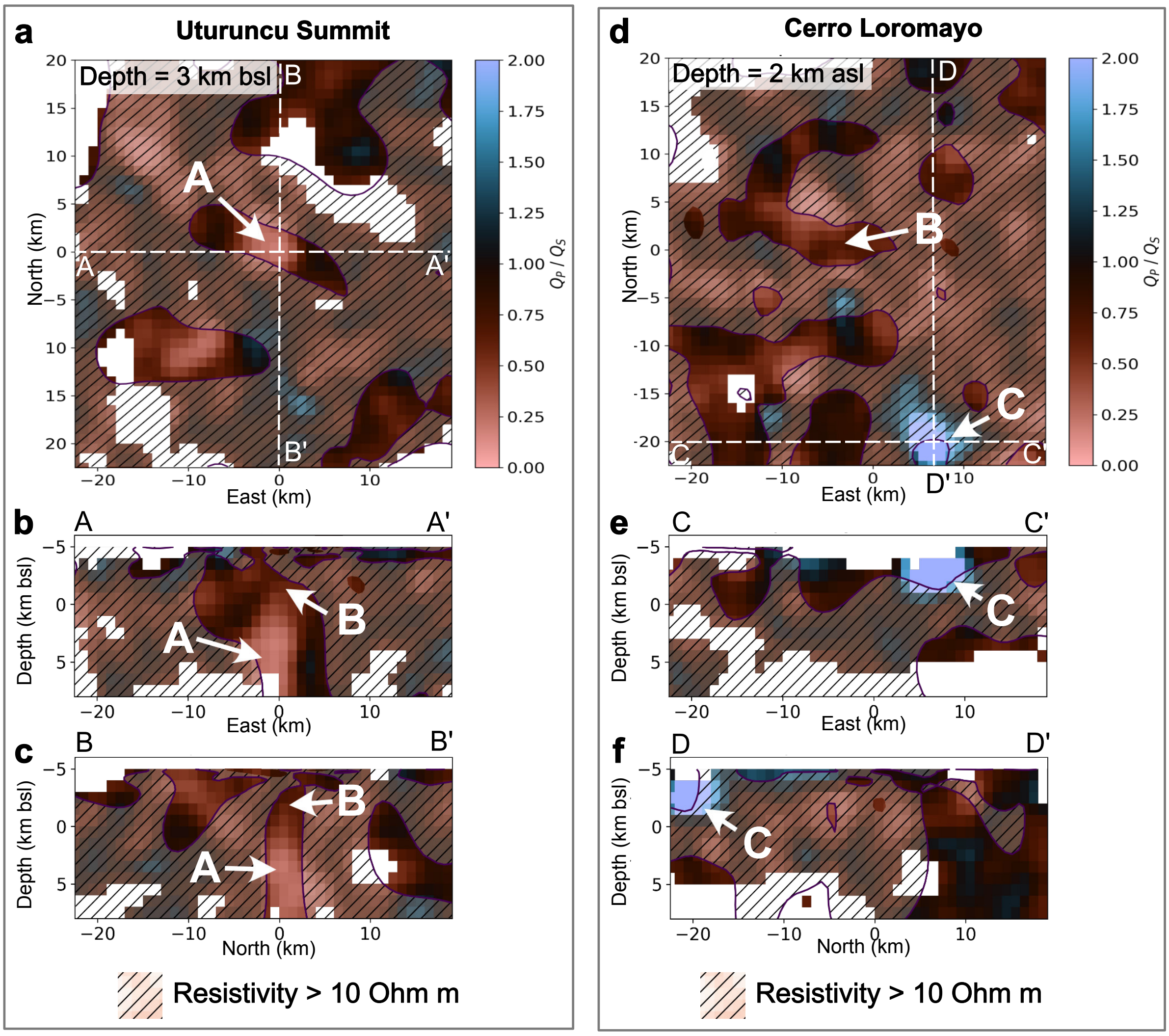

Figure 2. *Sections from the Q_P/Q_S tomography results, focussing on a $Q_P/Q_S < 1$ feature directly beneath Uturuncu and a $Q_P/Q_S > 1$ feature laterally offset to the South-East, beneath Cerro Loromayo. Results are overlaid with resistivity tomography results from* Comeau et al. (2016). *(a)-(c) Map and vertical cross-sections centred about the summit of Uturuncu. (d)-(f) Same as (a)-(c) except centred around a shallow, high QP/QS anomaly at Cerro Loromayo. Hashed regions are where resistivity >* 10 *Ω m, for which any brines would be low salinity or not present* (Afanasyev et al., 2018). *Labels A, to C are as referred to in Figure 4 and the Discussion. Results are masked as in Figure 1g-i.*

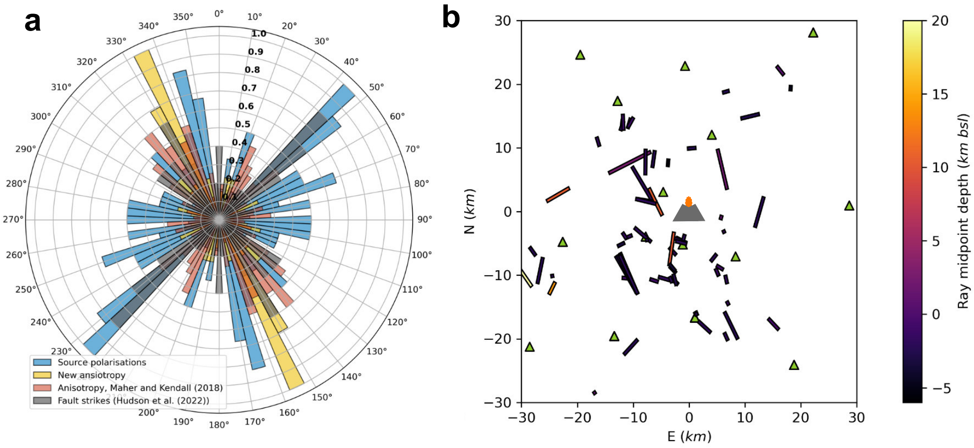

Figure 3. *Shear-wave velocity anisotropy results at Uturuncu volcano. (a) Rose diagram showing binned shear-wave velocity fast-directions and source polarisations from this study compared to fast-direction measurements from Maher and Kendall (2018) and fault strikes from Hudson et al. (2022). (b) Orientation of fast-direction for individual ray paths, plotted at ray mid-points of seismicity used in the shear-wave velocity anisotropy study. Lengths of the bars correspond to the delay times, δt. Volcano symbol indicates location of Uturuncu (0 km N, 0 km E) and green triangles are locations of receivers.*

Seismic anisotropy observations at Uturuncu are shown in Figure 3. The histograms in Figure 3a compare the orientations of the fast S-wave polarisation (yellow) to the source polarisations derived during the S-wave splitting analysis (blue), as well as fault strikes from Hudson et al. (2022) (grey) and previously published seismic anisotropy results (red) (Maher & Kendall, 2018). The fault strikes and source polarisations, which theoretically should be oriented fault-parallel, are primarily oriented SW-NE and NNW-SSE. However, the fast-directions are predominantly oriented NNW-SSE, with a minority of fast-directions oriented SW-NE lying to the north of Uturuncu (see Figure 3b). Data showing the orientation and strength of anisotropy with depth are plotted in Supplementary Figure 4, which suggest that the strength of anisotropy decreases as depth increases.

4 Discussion

4.1 Attenuation mechanisms

In order to make physical interpretations of the attenuation tomography, one first has to identify the dominant attenuation mechanism. Seismic attenuation is comprised of two contributions: intrinsic and extrinsic attenuation. Intrinsic attenuation is controlled by bulk medium properties, while extrinsic attenuation is typically controlled by features such as fractures. Methods for separating these two contributions do exist, underpinned by the comparison of direct P- and S- waves to highly-scattered coda using radiative transfer theory (Fehler et al., 1992; Hoshiba, 1991; Wang & Shearer, 2017; Wu, 1985). However, the application of such methods are limited for the Uturuncu dataset since: isolating the P-wave coda from the direct S-wave energy is challenging, thus making the separation of the dominant Q_P mechanism impossible; the method is highly dependent on the coda window length (Hoshiba, 1991); and results depend whether or not multiple scatterers and mode conversions are modelled, especially in volcanic environments (Yamamoto & Sato, 2010). Therefore, we instead attempt to identify the likely dominant attenuation mechanism, and what causes it, based on qualitative arguments.

Firstly, at depths shallower than 8 km bsl, high S-wave attenuation is confined to small pockets and high P- and S-wave attenuation are generally oriented in a narrow band with a strike NW-SE (see Figure 1). This band is parallel to the dominant fast-direction of the seismic anisotropy, as well as earthquake S-wave source polarizations and fault strikes. The high level of spatial variation in attenuation suggests that the dominant attenuation mechanism is due to interactions of the seismic waves with fault structures (i.e. extrinsic attenuation) rather than intrinsic attenuation, since the regional geology is unlikely to vary sufficiently to cause such high perturbations in intrinsic attenuation over such short length scales (Sparks et al., 2008). The attenuation structure deeper than 8 km bsl transitions to become approximately homogeneous, with anisotropy also decreasing with depth. This is likely partially due to resolution limits (see Supplementary Figure 2), but possibly also because at these depths the crust is too ductile to sustain sufficient fault structures required to promote significant scattering.

Assuming that the mechanism for the high attenuation regions is governed by the presence of fault structures, then a further question is what specifically causes the loss of seismic energy as the seismic waves interact with the faults. Fractures can scatter seismic energy due to reflection off the fracture interfaces (Zhu et al., 2007). Fluids in the pore space and along fractures can also cause attenuation due to mechanisms such as squirt flow (Chapman, 2003; Chapman et al., 2002). We suggest that fluids play an important role in facilitating the observed attenuation structure for the following reasons. Firstly, there are likely fluids ascending from the APMB, which sits directly beneath Uturuncu. The seismicity above the APMB has seismic b-values > 1 , consistent with fluids reducing fault normal stresses (Hudson et al., 2022). Further evidence is rooted in the observation that the high attenuation structures are oriented parallel to one set of fault orientations but not the other. There is evidence from both S-wave source polarisations and fault strikes that two sets of fault orientations exist, yet there is only one dominant direction exhibited in the seismic anisotropy and Q_P attenuation. We suggest that the crustal stress regime facilitates preferential opening of faults in one direction and closing of faults in the other, presumably governed locally (< 10 km from Uturuncu) by deformation at the volcano (Gottsmann et al., 2018; Pritchard et al., 2018) and regionally by tectonic stresses. This stress field would facilitate the ascent of fluids preferentially along one set of faults, causing the observed trend in anisotropy and attenuation. Additionally, a column of high P-wave attenuation (~5 km diameter, 10 km high) lies directly beneath Uturuncu, extending towards the APMB, with a column potentially observed in the S-wave attenuation too. The location of this column is in close agreement with a hypothesised route for fluid ascent (Gottsmann et al., 2017; Del Potro et al., 2013; Pritchard et al., 2018). Based on the above evidence, we suggest that the observed attenuation structures are predominantly caused by faults with fluids ascending and/or accumulating along them.

4.2 Identifying and mapping fluids and their composition

Assuming that the observed attenuation is primarily caused by fluids within faults, then relevant questions are what the fluid composition is and does it vary spatially. For simplicity we consider only three representative fluids: CO_2; H_2O (or analogous brines); and molten rock. Diagnostic data for addressing these questions are Q_P/Q_S ratios, which indicate whether the crust contains a proportion of fluids or gases that are compressible ($Q_P/Q_S < 1$) or the crust is fully-saturated with incompressible fluids ($Q_P/Q_S > 1$) (see Section 2.4 and Amalokwu et al. (2014); Chapman et al. (2021); Hauksson & Shearer (2006)). Additionally, pressure and temperature profiles, as well as resistivity data, can be used in combination with Q_P/Q_S to constrain fluid composition spatially. Figure 4 shows a schematic diagram summarising an inferred map of different fluids at Uturuncu based on the following discussion. Figure 4 also includes crustal pressure and temperature profiles (Pritchard et al., 2018 and references therein) and schematic compressibility and conductivity profiles that are used to further inform this discussion.

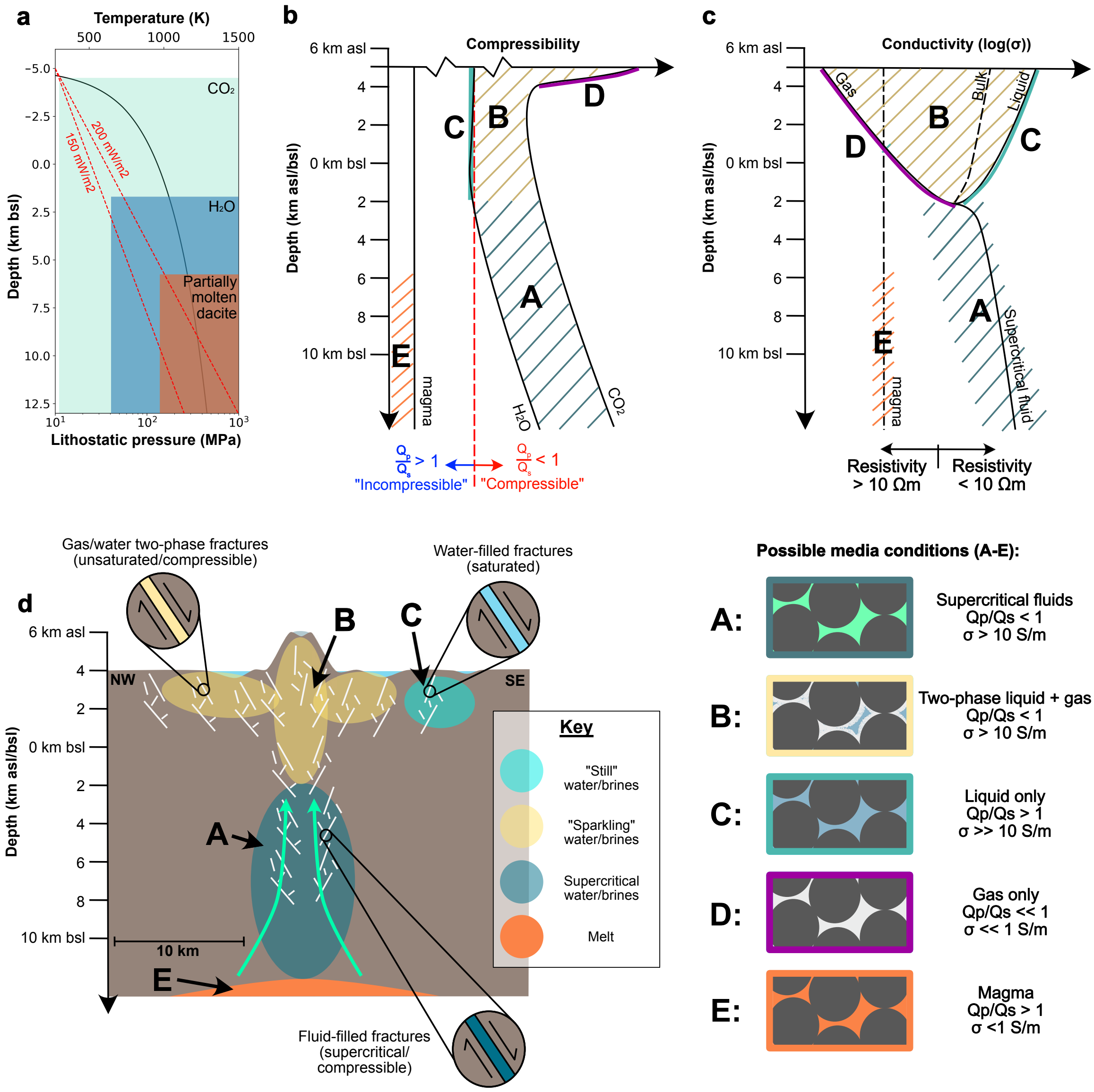

Figure 4. *Summary of our interpretations based on the seismic data presented in this study, as well as auxiliary data that informs our interpretation. a) Approximate pressure (black line) and temperature (red dashed lines) profiles with depth, based on data from Figure 2 of* Pritchard et al. (2018) *and references therein. Lithostatic pressure is calculated from density. Conditions where single-phase CO_2 and H_2O become supercritical are shown in light and dark blue, respectively. Conditions where partially molten dacite can be sustained are shown in orange, based on the dacite solidus calculated from the average of the temperature profiles* (Holtz et al., 2005; Pritchard et al., 2018). *b) Schematic depth profile of how fluid compressibility varies with depth. Compressibility profiles based partially on behaviour of CO_2* (Zhang et al., 2020). *c) Same as (b) but for conductivity, based partially on two-phase brine properties with increasing pressure* (Watanabe et al., 2021). *Conductivity of magma from* (Laumonier et al., 2017). *d) Schematic diagram summarising the key interpretations for different gas/fluid-filled fractures and the presence of brines beneath Uturuncu volcano.*

Below sea-level, features are less well resolved by the attenuation tomography than at shallower depths. However, one feature we are confident of is the $Q_P/Q_S << 1$ column directly beneath Uturuncu, labelled A in Figure 4 (also see Figure 2a-c), which extends from ~2 to 8 km bsl. This region of crust is highly faulted (Hudson et al., 2022), with Q_P/Q_S implying that these faults contain at least some compressible fluid component. Given the lithostatic pressures, it is unlikely that any gaseous phase is present at these depths. Intriguingly, H_2O becomes supercritical at these depths (see Figure 4a), driving the compressibility up and therefore Q_P/Q_S down (see Figure 4b). This feature has resistivities $< 10\ \Omega\ m$ (Comeau et al., 2016), consistent with high salinity brines (Afanasyev et al., 2018) (see Figure 4c) and not molten rock. These conductivities also rule out this feature being solely comprised of supercritical CO_2 (see Figure 4c). Furthermore, the sudden transition from a weak $Q_P/Q_S < 1$ signal to a strong $Q_P/Q_S << 1$ signal at ~2 km bsl, where H_2O/brines become supercritical, implies that this region contains at least some supercritical, compressible brine phase. However, this region of crust could also contain CO_2, or other volatiles, in combination with brines.

At depths shallower than sea-level, Q_P/Q_S ratios vary <1 (red regions, Figure 2, labelled B in Figure 4) and >1 (blue regions, Figure 2, labelled C in Figure 4), indicating that some regions of the shallow crust are partially saturated and others are fully saturated. This observation is expected <1 km from the surface, since this region of Bolivia is arid, yet surface snow and H_2O are present in places, which likely percolate into the shallow crust. However, saturated regions of the crust extend to depths at sea-level (>4 km below surface), too deep for groundwater aquifers. We interpret the regions in the vicinity of Uturuncu's summit with $Q_P/Q_S < 1$ and corresponding low resistivities (see label B, Figure 4b,d) as a 2-phase brine-CO_2 mixture, which could be referred to as "sparkling CO_2". These brines and CO_2 likely ascend from the APMB, via feature A, along faults in the crust.

Regions of $Q_P/Q_S > 1$, implying crust saturated with incompressible fluids, typically lie away from Uturuncu's summit. One particularly obvious example is that focussed on in Figure 2d-f, labelled C in Figure 4d. Again, the feature corresponds with low resistivities, indicative of high-salinity brines. This feature is therefore interpreted to be brine-saturated crust. Furthermore, this feature is particularly interesting as it lies beneath Cerro Loromayo (Fracchia, 2009; Soler et al., 2007), a volcano that could have exhibited activity as late as 0.9 Ma (Fracchia, 2009). Based on our Q_P/Q_S results, this feature appears isolated, with no vertical column-like feature below it. Furthermore, it corresponds to a low-density gravity anomaly (MacQueen et al., 2021), indicative of fluid accumulation. We therefore suggest that it is a brine-lens (Afanasyev et al., 2018) that was formed when Cerro Loromayo had an active hydrothermal system, but has subsequently cooled and is no longer fed by CO_2 or other volatiles from the APMB. Features such as this are exciting because they could potentially be a well-endowed accumulation of metal-rich brines (Blundy et al., 2021).

4.3 The bigger picture

Mapping what fluids accumulate where in the subsurface is important for numerous applications, including: volcanic hazard assessment; efficiently exploiting geothermal systems; and in searching for brines rich in metals critical for a green energy transition (Blundy et al., 2021). For volcanic hazard assessment, it is important to discriminate between hydrothermal and partial melt storage regions in order to accurately discriminate the volume of melt at a given volcano. Q_P/Q_S combined with temperature and pressure profiles makes this possible. Theoretically, our approach may also allow one to measure the proportion of melt, if densities are adequately constrained. For geothermal system characterisation, Q_P/Q_S can elucidate and map fluid-saturated crust vs. potentially dry crust, providing improved spatial constraint when targeting geothermal prospects. This constraint will reduce geothermal exploration risk. Similarly, Q_P/Q_S can also benefit the endeavour to find new, sustainable mineral resources in the form of metal-rich brines. Q_P/Q_S, in combination with temperature, pressure, density and conductivity profiles (Comeau et al., 2016; Del Potro et al., 2013; Ward et al., 2014), not only allows for the spatial constraint of metal-rich brine accumulation but also potentially the volume fraction of these brines within the crust. This information is critical for maximising the success of extracting metal-rich brines from geothermal systems going forward.

4.4 Limitations

A fundamental limitation of any tomographic method is the spatial resolution. This spatial resolution is governed by the density of ray path coverage, which is shown in Supplementary Figure S1. The P-wave coverage is significantly better than the S-wave coverage, owing to the greater number of picked P-wave arrivals. The Q_S and Q_P/Q_S tomography results are therefore limited, both in overall spatial extent and the minimum size of feature that can be resolved. The Q_P/Q_S results in Figure 3 are masked for regions where we are not confident that we can resolve features greater than 2 km in size. Significantly, we cannot observe the APMB with any confidence, primarily because only a small number of earthquakes from below the APMB are of sufficient quality to use in the attenuation tomography inversions. The resolution of the tomography could be improved by detecting more S-waves and/or increasing the number of stations in the network.

Another potential limitation is that we invert for Q_P^{-1} and Q_S^{-1} separately, producing our Q_P/Q_S tomographic map by division of each unit of the tomographic model individually, as in other studies (e.g. Hauksson & Shearer, 2006). However, this division method has two potential issues. Firstly, both Q_P^{-1} and Q_S^{-1} can take near-zero values for low-attenuation regions, which could lead to large variations in Q_P/Q_S. Secondly, even if the regularisation and smoothing parameters happen to be equal for both the Q_P and Q_S inversions, the resolution and associated uncertainty in the tomography results may differ. These issues can be mitigated by performing a direct inversion for Q_P/Q_S. We do not perform a direct inversion for Q_P/Q_S, as the complex velocity structure means that one cannot assume the same ray-path for a given P-wave and S-wave from the same source to the same receiver, a required condition if inverting directly for Q_P/Q_S using our method. Others have avoided this limitation by inverting for Q_P/Q_S by fixing Q_P using the Q_P tomography solution and then only varying Q_S in the inversion (Wei & Wiens, 2020). However, for our dataset, absolute values of Q_P/Q_S are highly dependent on the starting model. Instead, to maximise confidence in our direct division-derived Q_P/Q_S results, we mask out regions that have small Q_P^{-1} and/or Q_S^{-1} ($Q>500$) to minimise any near-zero division issues. We also minimise the effect of differing Q_P^{-1} and Q_S^{-1} resolution and uncertainties by masking out regions where either 4 km size Q_P or Q_S features cannot be resolved (see Supplementary Figures 1 and 2). We therefore have confidence in the remaining Q_P/Q_S results presented in Figure 2 and Figure 4.

A final limitation of note is the ambiguity of Q_P/Q_S ratios for identifying fluid type and the exact ratio of gas to liquid. Here, we require temperature and pressure profiles to identify the most likely fluid/s associated with a given Q_P/Q_S ratio. However, pressure and temperature profiles may well be inaccurate, especially as they only describe variations in one-dimension, depth. V_P, V_S and V_P/V_S results could provide additional constraint, although velocity is less sensitive to fluid saturation than attenuation (Winkler & Nur, 1982). Other geophysical measurements such as density (Del Potro et al., 2013; Ward et al., 2014) would provide additional constraint, which in combination with other parameters might constrain porosity. However, one particularly useful observation would be resistivity tomography (Comeau et al., 2016), which would aid constraint of the presence of conductive brines vs. resistive gases. Ideally, one would perform a joint inversion, including all these parameters to simultaneously constrain additional parameters, such as porosity, conductivity and density, in order to identify fluid composition and prevalence better.

5. Conclusions

We present seismic attenuation and anisotropy results at Uturuncu volcano, Bolivia. 3D attenuation tomography shows higher-than-background P-wave attenuating structures that align parallel to the orientation of fractures (NNW-SSE). The presence and orientation of these fractures is evidenced by seismic anisotropy. Higher-than-background S-wave attenuation is isolated to smaller localities, sporadically located along the strike of the high P-wave attenuation regions. Q_P/Q_S ratios, indicative of crustal fluid saturation, show that most of the crust is partially saturated, with only a few pockets of fully-saturated crust. We interpret saturated crust above sea-level to be brine saturated crust in its normal state, likely a brine lens that developed during active volcanism that has now ceased. A column of particularly low Q_P/Q_S directly beneath Uturuncu is interpreted to comprise of supercritical fluids, most likely H_2O or metal-rich brines, potentially containing volatiles. This likely feeds CO_2 and other volatiles into a shallow hydrothermal system.

We show that high seismic attenuation features can be attributed to fluid accumulation along faults, if constrained by other observations such as seismic anisotropy. Furthermore, if one has constraint over pressure and temperature profiles through the crust, as well as data constraining crustal resistivity, then it is possible to identify the most likely fluid compositions responsible for each seismic attenuation signature. We therefore conclude that fluid accumulation and composition can be mapped seismically. Such observations at other locations could be used for a range of applications, from volcanic hazard assessment to the exploration of metal-rich brine deposits that could potentially be exploited to facilitate the green-energy transition.

Acknowledgements

We thank all the PLUTONS team for fruitful discussions. We especially thank Ying Liu for providing the seismic velocity model that was used to locate the seismicity in this study. The seismic data analysed in this study is publicly available from IRIS, with the earthquake catalogue used described in Hudson et al. (2022). The software used to measure path-average attenuation for each earthquake is SeisSrcMoment (Hudson, 2020), available open source. The shear-wave splitting analysis was undertaken using SWSPy (Hudson, 2022), another open source package. Some of the figures were produced using Generic Mapping Tools (GMT) (Wessel et al., 2019). Much of the seismic data analysis was performed using ObsPy (Beyreuther et al., 2010). This work, and TSH were funded by the NSFGEO-NERC grant NE/S008845/1. JDB thanks the Royal Society for financial support through a Research Professorship (RP\R1\201048). MEP was funded by National Science Foundation grant EAR-1757495. SSW was funded by US National Science Foundation grant EAR-2042553. The seismic data collection funded by the US National Science Foundation grants 0908281 and 0909254, and the UK Natural Environment Research Council grant NE/G01843X/1.

References

Afanasyev, A., Blundy, J., Melnik, O., & Sparks, S. (2018). Formation of magmatic brine lenses via focussed fluid-flow beneath volcanoes. *Earth and Planetary Science Letters*, *486*, 119–128. https://doi.org/10.1016/j.epsl.2018.01.013

Aki, K., & Richards, P. G. (2002). *Quantitative Seismology*. University Science Books.

Amalokwu, K., Best, A. I., Sothcott, J., Chapman, M., Minshull, T., & Li, X. Y. (2014). Water saturation effects on elastic wave attenuation in Porous rocks with aligned fractures. *Geophysical Journal International*, *197*(2), 943–947. https://doi.org/10.1093/gji/ggu076

Bacon, C. A., Johnson, J., White, R. S., & Rawlinson, N. (2021). On the origin of seismic anisotropy in the shallow crust of the Northern Volcanic Zone , Iceland.

Baird, A. F., Kendall, J. M., Sparks, R. S. J., & Baptie, B. (2015). Transtensional deformation of Montserrat revealed by shear wave splitting. *Earth and Planetary Science Letters*, *425*, 179–186. https://doi.org/10.1016/j.epsl.2015.06.006

Blundy, J., Afanasyev, A., Tattitch, B., Sparks, S., Melnik, O., Utkin, I., & Rust, A. (2021). The economic potential of metalliferous sub-volcanic brines. *Royal Society Open Science*, *8*(6). https://doi.org/10.1098/rsos.202192

Bohm, M., Haberland, C., & Asch, G. (2013). Imaging fluid-related subduction processes beneath Central Java (Indonesia) using seismic attenuation tomography. *Tectonophysics*, *590*, 175–188. https://doi.org/10.1016/j.tecto.2013.01.021

Brune, J. N. (1970). Tectonic Stress and the Spectra of Seismic Shear Waves from Earthquakes. *Journal of Geophysical Research*, *75*(26), 4997–5009.

Caudron, C., Girona, T., Taisne, B., Suparjan, Gunawan, H., Kristianto, & Kasbani. (2019). Change in seismic attenuation as a long-term precursor of gas-driven eruptions. *Geology*, *47*(7), 632–636. https://doi.org/10.1130/G46107.1

Chapman, M. (2003). Frequency-dependent anisotropy due to meso-scale fractures in the presence of equant porosity. *Geophysical Prospecting*, *51*(5), 369–379. https://doi.org/10.1046/j.1365-2478.2003.00384.x

Chapman, M., Zatsepin, S. V., & Crampin, S. (2002). Derivation of a microstructural poroelastic model. *Geophysical Journal International*, *151*(2), 427–451. https://doi.org/10.1046/j.1365-246X.2002.01769.x

Chapman, S., Borgomano, J. V. M., Quintal, B., Benson, S. M., & Fortin, J. (2021). Seismic Wave Attenuation and Dispersion Due to Partial Fluid Saturation: Direct Measurements and Numerical Simulations Based on X-Ray CT. *Journal of Geophysical Research: Solid Earth*, *126*(4), 1–26. https://doi.org/10.1029/2021JB021643

Comeau, M. J., Unsworth, M. J., & Cordell, D. (2016). New constraints on the magma distribution and composition beneath Volcán Uturuncu and the southern Bolivian Altiplano from magnetotelluric data. *Geosphere*, *12*(5), 1391–1421. https://doi.org/10.1130/GES01277.1

Crampin, S. (1981). A review of wave motion in anisotropic and cracked elastic-media. *Wave Motion*, *3*(4), 343–391. https://doi.org/10.1016/0165-2125(81)90026-3

Fehler, M., Hoshiba, M., Sato, H., & Obara, K. (1992). Separation of scattering and intrinsic attenuation for the Kanto-Tokai region, Japan, using measurements of S-wave energy versus hypocentral distance. *Geophysical Journal International*, *108*(3), 787–800. https://doi.org/10.1111/j.1365-246X.1992.tb03470.x

Fracchia, D. (2009). Volcanismo postcolapso de la caldera Vilama , Mioceno superior , Mecanismos eruptivos y Petrogénesis. Tesis Doctoral.

Gerst, A., & Savage, M. K. (2004). Seismic anisotropy beneath Ruapehu Volcano: A possible eruption forecasting tool. *Science*, *306*(5701), 1543–1547. https://doi.org/10.1126/science.1103445

Gottsmann, J., Blundy, J., Henderson, S., Pritchard, M. E., & Sparks, R. S. J. (2017). Thermomechanical modeling of the altiplano-puna deformation anomaly: Multiparameter insights into magma mush reorganization. *Geosphere*, *13*(4), 1042–1045. https://doi.org/10.1130/GES01420.1

Gottsmann, J, Eiden, E., & Pritchard, M. E. (2022). Transcrustal compressible fluid flow explains the Altiplano-Puna gravity and deformation anomalies. *Geophysical Research Letters*, 1–16.

Gottsmann, Joachim, del Potro, R., & Muller, C. (2018). 50 years of steady ground deformation in the Altiplano-Puna region of southern Bolivia. *Geosphere*, *14*(1), 65–73. https://doi.org/10.1130/GES01570.1

Gudmundsson, Ó., Finlayson, D. M., Itikarai, I., Nishimura, Y., & Johnson, W. R. (2004). Seismic attenuation at Rabaul volcano, Papua New Guinea. *Journal of Volcanology and Geothermal Research*, *130*(1–2), 77–92. https://doi.org/10.1016/S0377-0273(03)00282-8

Hauksson, E., & Shearer, P. M. (2006). Attenuation models (QP and QS) in three dimensions of the southern California crust: Inferred fluid saturation at seismogenic depths. *Journal of Geophysical Research: Solid Earth*, *111*(5), 1–21. https://doi.org/10.1029/2005JB003947

Holtz, F., Sato, H., Lewis, J., Behrens, H., & Nakada, S. (2005). Experimental petrology of the 1991-1995 Unzen dacite, Japan. Part I: Phase relations, phase composition and pre-eruptive conditions. *Journal of Petrology*, *46*(2), 319–337. https://doi.org/10.1093/petrology/egh077

Hoshiba, M. (1991). Simulation of multiple-scattered coda wave excitation based on the energy conservation law. *Physics of the Earth and Planetary Interiors*, *67*(1–2), 123–136. https://doi.org/10.1016/0031-9201(91)90066-Q

Hudson, T.S. (2020). TomSHudson/SeisSrcMoment: First formal release (Version 1.0.0). *Zenodo*. https://doi.org/http://doi.org/10.5281/zenodo.4010325

Hudson, Thomas S., Kendall, J. M., Pritchard, M. E., Blundy, J. D., & Gottsmann, J. H. (2022). From slab to surface: Earthquake evidence for fluid migration at Uturuncu volcano, Bolivia. *Earth and Planetary Science Letters*, *577*, 117268. https://doi.org/10.1016/j.epsl.2021.117268

Hudson, Thomas S, Smith, J., Brisbourne, A., & White, R. (2019). Automated detection of basal icequakes and discrimination from surface crevassing. *Annals of Glaciology*, *60*(79), 1–11.

Hudson, Thomas Samuel. (2022). SWSPy release 1.0.0. *Zenodo*. https://doi.org/10.5281/zenodo.7007408

Johnson, J. H., Savage, M. K., & Townend, J. (2011). Distinguishing between stress-induced and structural anisotropy at Mount Ruapehu volcano, New Zealand. *Journal of Geophysical Research: Solid Earth*, *116*(12), 1–18. https://doi.org/10.1029/2011JB008308

Kendall, J. M. (2000). Seismic anisotropy in the boundary layers of the mantle. *Geophysical Monograph Series*, *117*, 133–159. https://doi.org/10.1029/GM117p0133

Klimentos, T. (1995). Attenuation of P - and S -waves as a method of distinguishing gas and condensate from oil and water. *GEOPHYSICS*, *60*(2), 447–458. https://doi.org/10.1190/1.1443782

Krischer, L. (2016). mtspec Python wrappers 0.3.2. *Zenodo*. https://doi.org/10.5281/zenodo.321789

Kukarina, E., West, M., Keyson, L. H., Koulakov, I., Tsibizov, L., & Smirnov, S. (2017). Focused magmatism beneath Uturuncu volcano, Bolivia: Insights from seismic tomography and deformation modeling. *Geosphere*, *13*(6), 1855–1866. https://doi.org/10.1130/GES01403.1

Lanza, F., Thurber, C. H., Syracuse, E. M., Power, J. A., & Ghosh, A. (2020). Seismic tomography of compressional wave velocity and attenuation structure for Makushin Volcano, Alaska. *Journal of Volcanology and Geothermal Research*, *393*, 106804. https://doi.org/10.1016/j.jvolgeores.2020.106804

Laumonier, M., Gaillard, F., Muir, D., Blundy, J., & Unsworth, M. (2017). Giant magmatic water reservoirs at mid-crustal depth inferred from electrical conductivity and the growth of the continental crust. *Earth and Planetary Science Letters*, *457*, 173–180. https://doi.org/10.1016/j.epsl.2016.10.023

Lees, J. M. (2007). Seismic tomography of magmatic systems. *Journal of Volcanology and Geothermal Research*, *167*(1–4), 37–56. https://doi.org/10.1016/j.jvolgeores.2007.06.008

Lelièvre, P. G., Farquharson, C. G., & Hurich, C. A. (2011). Computing first-arrival seismic traveltimes on unstructured 3-D tetrahedral grids using the Fast Marching Method. *Geophysical Journal International*, *184*(2), 885–896. https://doi.org/10.1111/j.1365-246X.2010.04880.x

Lomax, A., & Virieux, J. (2000). Probabilistic earthquake location in 3D and layered models. *Advances in Seismic Event Location, Volume 18 of the Series Modern Approaches in Geophysics*, 101–134.

MacQueen, P., Gottsmann, J., Pritchard, M. E., Young, N., Ticona J, F., Ticona, E., & Tintaya, R. (2021). Dissecting a Zombie: Joint Analysis of Density and Resistivity Models Reveals Shallow Structure and Possible Sulfide Deposition at Uturuncu Volcano, Bolivia. *Frontiers in Earth Science*, *9*(September), 1–20. https://doi.org/10.3389/feart.2021.725917

Maher, S., & Kendall, J. M. (2018). Crustal anisotropy and state of stress at Uturuncu Volcano, Bolivia, from shear-wave splitting measurements and magnitude–frequency distributions in seismicity. *Earth and Planetary Science Letters*, *495*, 38–49. https://doi.org/10.1016/j.epsl.2018.04.060

Muir, D. D., Barfod, D. N., Blundy, J. D., Rust, A. C., Sparks, R. S. J., & Clarke, K. M. (2015). The temporal record of magmatism at Cerro Uturuncu, Bolivian Altiplano. *Geological Society Special Publication*, *422*(1), 57–83. https://doi.org/10.1144/SP422.1

Nasr, M., Giroux, B., & Dupuis, J. C. (2020). A hybrid approach to compute seismic travel times in three-dimensional tetrahedral meshes. *Geophysical Prospecting*, *68*(4), 1291–1313. https://doi.org/10.1111/1365-2478.12930

Nowacki, A., Wilks, M., Kendall, J. M., Biggs, J., & Ayele, A. (2018). Characterising hydrothermal fluid pathways beneath Aluto volcano, Main Ethiopian Rift, using shear wave splitting. *Journal of Volcanology and Geothermal Research*, *356*, 331–341. https://doi.org/10.1016/j.jvolgeores.2018.03.023

O'Brien, G. S., & Bean, C. J. (2009). Volcano topography, structure and intrinsic attenuation: Their relative influences on a simulated 3D visco-elastic wavefield. *Journal of Volcanology and Geothermal Research*, *183*(1–2), 122–136. https://doi.org/10.1016/j.jvolgeores.2009.03.004

Del Pezzo, E., Ibanez, J., Morales, J., Akinci, A., & Maresca, R. (1995). Measurements of intrinsic and scattering seismic attenuation in the crust. *Bulletin - Seismological Society of America*, *85*(5), 1373–1380. https://doi.org/10.1785/bssa0850051373

Del Potro, R., Díez, M., Blundy, J., Camacho, A. G., & Gottsmann, J. (2013). Diapiric ascent of silicic magma beneath the Bolivian Altiplano. *Geophysical Research Letters*, *40*(10), 2044–2048. https://doi.org/10.1002/grl.50493

Prieto, G. A., Parker, R. L., & Vernon, F. L. (2009). A Fortran 90 library for multitaper spectrum analysis. *Computers and Geosciences*, *35*(8), 1701–1710. https://doi.org/10.1016/j.cageo.2008.06.007

Pritchard, M. E., de Silva, S. L., Michelfelder, G., Zandt, G., McNutt, S. R., Gottsmann, J., et al. (2018). Synthesis: PLUTONS: Investigating the relationship between pluton growth and volcanism in the Central Andes. *Geosphere*, *14*(3), 954–982. https://doi.org/10.1130/GES01578.1

Rawlinson, N., & Spakman, W. (2016). On the use of sensitivity tests in seismic tomography. *Geophysical Journal International*, *205*(2), 1221–1243. https://doi.org/10.1093/gji/ggw084

Rawlinson, Nicholas, & Sambridge, M. (2005). The fast marching method: an effective tool for tomographic imaging and tracking multiple phases in complex layered media. *Exploration Geophysics*, *36*, 341–350. https://doi.org/10.1071/EG05341

Sanders, C. O., Ponko, S. C., Nixon, L. D., & Schwartz, E. A. (1995). Seismological evidence for magmatic and hydrothermal structure in Long Valley Caldera from local earthquake attenuation and velocity tomography. *Journal of Geophysical Research: Solid Earth*, *100*(B5), 8311–8326. https://doi.org/10.1029/95JB00152

De Siena, L., Thomas, C., & Aster, R. (2014). Multi-scale reasonable attenuation tomography analysis (MuRAT): An imaging algorithm designed for volcanic regions. *Journal of Volcanology and Geothermal Research*, *277*, 22–35. https://doi.org/10.1016/j.jvolgeores.2014.03.009

Silver, P. G., & Chan, W. W. (1991). Shear Wave Splitting and Sub continental Mantle Deformation. *Journal of Geophysical Research*, *96*, 429–454. https://doi.org/10.1029/91JB00899

Smith, J. D., White, R. S., Avouac, J.-P., & Bourne, S. (2020). Probabilistic earthquake locations of induced seismicity in the Groningen region, the Netherlands. *Geophysical Journal International*, *222*(1), 507–516. https://doi.org/10.1093/gji/ggaa179

Soler, M. M., Caffe, P. J., Coira, B. L., Onoe, A. T., & Kay, S. M. (2007). Geology of the Vilama caldera: A new interpretation of a large-scale explosive event in the Central Andean plateau during the Upper Miocene. *Journal of Volcanology and Geothermal Research*, *164*(1–2), 27–53. https://doi.org/10.1016/j.jvolgeores.2007.04.002

Sparks, R. S. J., Folkes, C. B., Humphreys, M. C. S., Barfod, D. N., Clavero, J., Sunagua, M. C., et al. (2008). Uturuncu volcano, Bolivia: Volcanic unrest due to mid-crustal magma intrusion. *American Journal of Science*, *308*(6), 727–769. https://doi.org/10.2475/06.2008.01

Teanby, N. A., Kendall, J., & Baan, M. Van Der. (2004). Automation of Shear-Wave Splitting Measurements using Cluster Analysis. *Bulletin of the Seismological Society of America*, *94*(2), 453–463.

Thomas, C., & Kendall, J.-M. (2002). The lowermost mantle beneath northern Asia-II. Evidence for lower-mantle anisotropy. *Geophysical Journal International*, *151*(1), 296–308. https://doi.org/10.1046/j.1365-246X.2002.01760.x

Walsh, E., Arnold, R., & Savage, M. K. (2013). Silver and Chan revisited. *Journal of Geophysical Research: Solid Earth*, *118*(10), 5500–5515. https://doi.org/10.1002/jgrb.50386

Wang, W., & Shearer, P. M. (2017). Using direct and coda wave envelopes to resolve the scattering and intrinsic attenuation structure of Southern California. *Journal of Geophysical Research: Solid Earth*, *122*(9), 7236–7251. https://doi.org/10.1002/2016JB013810

Ward, K. M., Zandt, G., Beck, S. L., Christensen, D. H., & McFarlin, H. (2014). Seismic imaging of the magmatic underpinnings beneath the Altiplano-Puna volcanic complex from the joint inversion of surface wave dispersion and receiver functions. *Earth and Planetary Science Letters*, *404*, 43–53. https://doi.org/10.1016/j.epsl.2014.07.022

Watanabe, N., Yamaya, Y., Kitamura, K., & Mogi, T. (2021). Viscosity-dependent empirical formula for electrical conductivity of H2O-NaCl fluids at elevated temperatures and high salinity. *Fluid Phase Equilibria*, *549*, 113187. https://doi.org/10.1016/j.fluid.2021.113187

Wei, S. S., & Wiens, D. A. (2018). P-wave attenuation structure of the Lau back-arc basin and implications for mantle wedge processes. *Earth and Planetary Science Letters*, *502*, 187–199. https://doi.org/10.1016/j.epsl.2018.09.005

Wei, S. S., & Wiens, D. A. (2020). High Bulk and Shear Attenuation Due to Partial Melt in the Tonga-Lau Back-arc Mantle. *Journal of Geophysical Research: Solid Earth*, *125*(1), 1–16. https://doi.org/10.1029/2019JB017527

Winkler, K., & Nur, A. (1979). Pore fluids and seismic attenuation in rocks. *Geophysical Research Letters*, *6*(1), 1–4. https://doi.org/10.1029/GL006i001p00001

Winkler, K. W., & Nur, A. (1982). Seismic attenuation: effects of pore fluids and frictional sliding. *Geophysics*, *47*(1), 1–15. https://doi.org/10.1190/1.1441276

Wu, R. -S. (1985). Multiple scattering and energy transfer of seismic waves – separation of scattering effect from intrinsic attenuation – I. Theoretical modelling. *Geophysical Journal of the Royal Astronomical Society*, *82*(1), 57–80. https://doi.org/10.1111/j.1365-246X.1985.tb05128.x

Yamamoto, M., & Sato, H. (2010). Multiple scattering and mode conversion revealed by an active seismic experiment at Asama volcano, Japan. *Journal of Geophysical Research: Solid Earth*, *115*(7). https://doi.org/10.1029/2009JB007109

Zhang, P., Celia, M. A., Bandilla, K. W., Hu, L., & Meegoda, J. N. (2020). A Pore-Network Simulation Model of Dynamic CO2 Migration in Organic-Rich Shale Formations. *Transport in Porous Media*, *133*(3), 479–496. https://doi.org/10.1007/s11242-020-01434-9

Zhao, D. (2001). Seismological structure of subduction zones and its implications for arc magmatism and dynamics. *Physics of the Earth and Planetary Interiors*, *127*(1–4), 197–214. https://doi.org/10.1016/S0031-9201(01)00228-X

Zhu, Y., Tsvankin, I., Dewangan, P., & Wijk, K. van. (2007). Physical modeling and analysis of P-wave attenuation anisotropy in transversely isotropic media. *GEOPHYSICS*, *72*(1), D1–D7. https://doi.org/10.1190/1.2374797

Geophysical Research Letters

Supporting Information for

Hydrothermal fluids and where to find them: Using seismic attenuation an anisotropy to map fluids beneath Uturuncu volcano, Bolivia

T.S. Hudson[1], JM. Kendall[1], J.D. Blundy[1], M.E. Pritchard[2], P. MacQueen[2], S.S. Wei[3], J.H. Gottsmann[4], S. Lapins[4]

[1]Department of Earth Sciences, University of Oxford, UK

[2]Department of Earth and Atmospheric Sciences, Cornell University, USA

[3]Department of Earth and Environmental Sciences, Michigan State University, USA

[4]School of Earth Sciences, University of Bristol, UK

Contents of this file

Introduction

Here, we provide exact details of how the attenuation tomography and S-wave velocity anisotropy analysis was performed. We also include supplementary figures showing: the earthquake catalogue, tomography resolution tests, the magnetotelluric data from the literature, and additional seismic anisotropy results.

Supplementary Text 1: Attenuation tomography

Attenuation tomography comprises of using path-averaged attenuation observations, Q_{path}, between earthquake sources and receivers, to map the attenuation structure. The 3D attenuation tomography performed in this study is undertaken using the earthquakes and receivers shown in Figure 1, with the ray paths shown in Supplementary Figure S1. Our method is based upon that described in (Wei & Wiens, 2018) with some alterations, required due to the local nature of the study area. The critical observation we require to perform this inversion is the path-averaged attenuation, $\bar{Q}_{path}$, which is related to t*, given by,

$$t_i^* = \frac{t_i}{\bar{Q}_{path,i}} \quad ,$$

where t_i is the travel time of the seismic phase from the source to the receiver for earthquake ***i***. We obtain t*, and hence $\bar{Q}_{path}$, for each earthquake by calculating the displacement spectrum of the earthquake. We then assume that the source can be described by the Brune model (Brune, 1970), which is given by,

$$\Omega(f) = \frac{\Omega_0 e^{-\pi f t^*}}{\left(1 + \left(\frac{f}{f_c}\right)^2\right)} \quad ,$$

where ***f*** is the frequency, f_c is the corner frequency and Ω_0 is the long-period spectral amplitude. To find t*, we vary the parameters f_c, t*, and Ω_0 to find the Brune model that best matches the observed displacement spectrum for each earthquake source-receiver pair.

The observed t* values for all source-receiver pairs can then be used to perform a tomographic inversion to image the attenuation structure. The equation describing this tomography inversion is given by (Wei & Wiens, 2018),

$$t_i^* = \sum_{j=1}^{j=n_{nodes}} \frac{l_{ij}}{v_j} \frac{1}{Q_j} = G_{ij} m_j \quad ,$$

where n_{nodes} is the number of nodes in the 3D grid, l_{ij} is the path length for a ray associated with source-receiver pair i through node j, v_j is the seismic velocity of node j, Q_j is the quality factor measure of attenuation in node j, G_{ij} is the tomography tensor component associated with the source-receiver pair i and node j, and m_j is the tomography model attenuation for node j, where $m_j = \frac{1}{Q_j}$. The above equation can be rewritten in tensor notation as,

$$\boldsymbol{t}^* = \boldsymbol{G}.\boldsymbol{m} \quad ,$$

where $\boldsymbol{t}^*$ is a vector of length n_{pairs}, the number of source-receiver pairs, $\boldsymbol{G}$ is a second order tensor, and $\boldsymbol{m}$ is a vector of length n_{nodes}. We can solve this equation to find the model attenuation vector, $\boldsymbol{m}$, by performing a regularised linear least-squares inversion. This attenuation tomography method can be applied to P or S seismic phases to obtain Q_P or Q_S, respectively.

The above theory is implemented practically through the specific attenuation tomography steps as follows:

1. First we calculate the t_i^* measurements for each source-receiver pair to find $\boldsymbol{t}^*$. To do this we take a window around the P or S phase and compute the observed displacement spectrum using the multi-taper spectrum method of Krischer (2016) and Prieto et al. (2009). We then find the best-fitting Brune model to find the best estimates of $f_{c,i}$, t_i^*, and $\Omega_{0,i}$ for that source-receiver path. We repeat this for every source-receiver path to find $\boldsymbol{t}^*$. The Brune model does not always adequately fit the observed displacement spectrum. We filter out poor fits by removing source-receiver pairs associated with events that have a standard deviation in $\bar{Q}_{path}$, $\sigma_{\bar{Q}_{path}}$, greater than 400.

2. We then specify the 3D grid nodes for the tomographic inversion. We use a ***120 km*** by ***120 km*** by ***60 km*** grid with a uniform grid spacing of 1 km. We include the receivers inside the grid, with the adjacent nodes implicitly accommodating any local site effects in the tomographic inversion.
3. We then perform ray tracing to calculate the path lengths, l_{ij}, through each cell. We use the ray tracing code (Nasr et al., 2020), which uses the fast marching method (Lelièvre et al., 2011; Nicholas Rawlinson & Sambridge, 2005).
4. The final component we require to perform the tomographic inversion is the tomography tensor, **G**. This second order tensor is given by,

$$\boldsymbol{G} = \begin{pmatrix} \frac{l_{11}}{v_1} & \cdots & \frac{l_{1j}}{v_j} \\ \vdots & \ddots & \vdots \\ \frac{l_{i1}}{v_1} & \cdots & \frac{l_{ij}}{v_j} \end{pmatrix} .$$

5. We can then perform the regularised linear least squares inversion, which involves minimising the function,

$$f(\boldsymbol{m}) = \|\boldsymbol{Gm} - \boldsymbol{t}^*\|_2^2 + \lambda\|\boldsymbol{m}\| \quad ,$$

   where λ is the regularisation coefficient. To find the optimal regularisation so as to avoid under- or over-fitting, we perform the inversion for multiple values of λ and select the value of λ at the corner of the L-curve. This provides us with the best fitting attenuation model ***m***.
6. The best fitting attenuation model may have physically unrealistic jumps in attenuation between individual cells. We account for this by applying smoothing to the model to produce a final, realistic attenuation model. There are various ways of applying smoothing to a tomography model. We apply 2D Gaussian smoothing over a wavelength of 1 km to each xy-plane layer in the 3D model. We apply lateral rather than vertical 2D smoothing since we are primarily interested in the attenuation variation with depth, and so do not want to introduce any unnecessary bias to the tomography result in this axis.

The steps to obtain t* measurements are implemented in the open source python code SeisSrcMoment (Hudson, 2020).

Supplementary Text 2: Seismic anisotropy

Seismic anisotropy in this study refers to S-wave velocity anisotropy. Such anisotropy can be broadly attributed to two factors: crystallographic orientation, where individual crystals of the medium preferentially align; and bulk-fabric anisotropy, typically caused by the preferential alignment of fractures that may be fluid-filled. Seismic anisotropy manifests itself as follows. An S-wave radiated from an earthquake source will have an initial polarisation. For a double-couple source, this polarisation is parallel to the slip-direction of the fault generating the earthquake. If a region of the crust is seismically anisotropic, then as the S-wave propagates through this region, the energy will be partitioned into two orthogonal components, one oriented in the plane of the fast-direction, ϕ, and the other in the plane of the slow-direction. Stronger anisotropy or a longer ray path through the anisotropic region will result in greater delay-times between these fast and slow S-waves . This phenomenon is called shear-wave splitting (Crampin, 1981; Silver & Chan, 1991). Shear-wave splitting is measured using SWSPy (Hudson, 2022), which is based on the eigenvalue method described in Teanby et al. (2004) and Walsh et al. (2013). The strength of anisotropy is quantified by the delay-time, δt. However, it is also useful to measure the strength of anisotropy, a, as the magnitude of splitting normalised by the distance travelled (Thomas & Kendall, 2002). If the delay time is defined by,

$$\delta t = t_{slow} - t_{fast} = \frac{d}{\bar{v}\left(1 - \frac{a}{2}\right)} - \frac{d}{\bar{v}\left(1 + \frac{a}{2}\right)} \quad ,$$

where d is the ray path length and $\bar{v}$ is the mean velocity of the medium, then the magnitude of anisotropy is given by (Thomas & Kendall, 2002),

$$a = \delta v_S = -\frac{2d}{\bar{v}\delta t} \pm \sqrt{\left(\frac{2d}{\bar{v}\delta t}\right)^2 + 4} \quad .$$

Supplementary figures

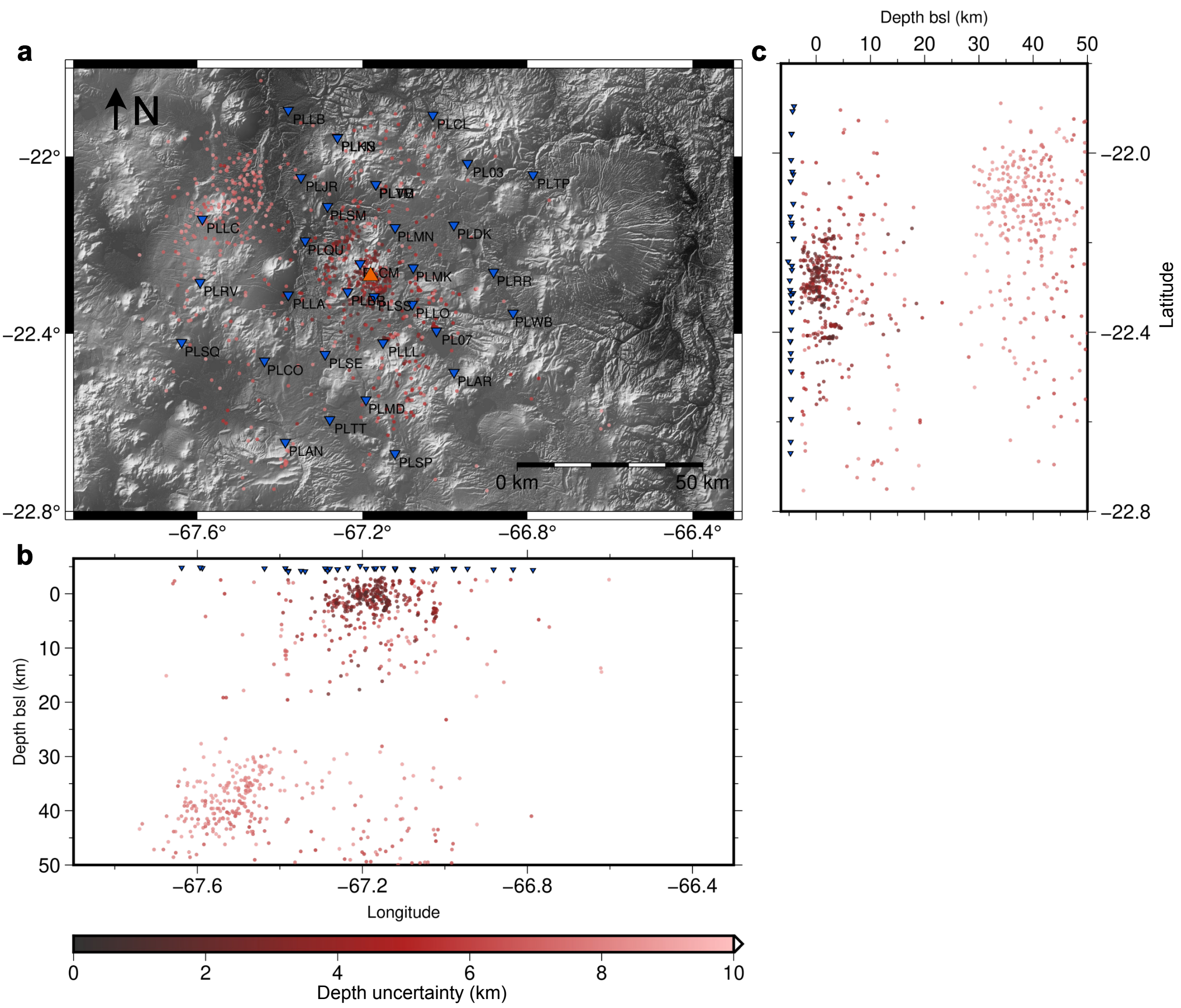

Supplementary Figure 1. Seismicity used in this study. Blue inverted triangles show seismometer locations. Red scatter points show earthquake hypocentres, coloured by uncertainty in depth.

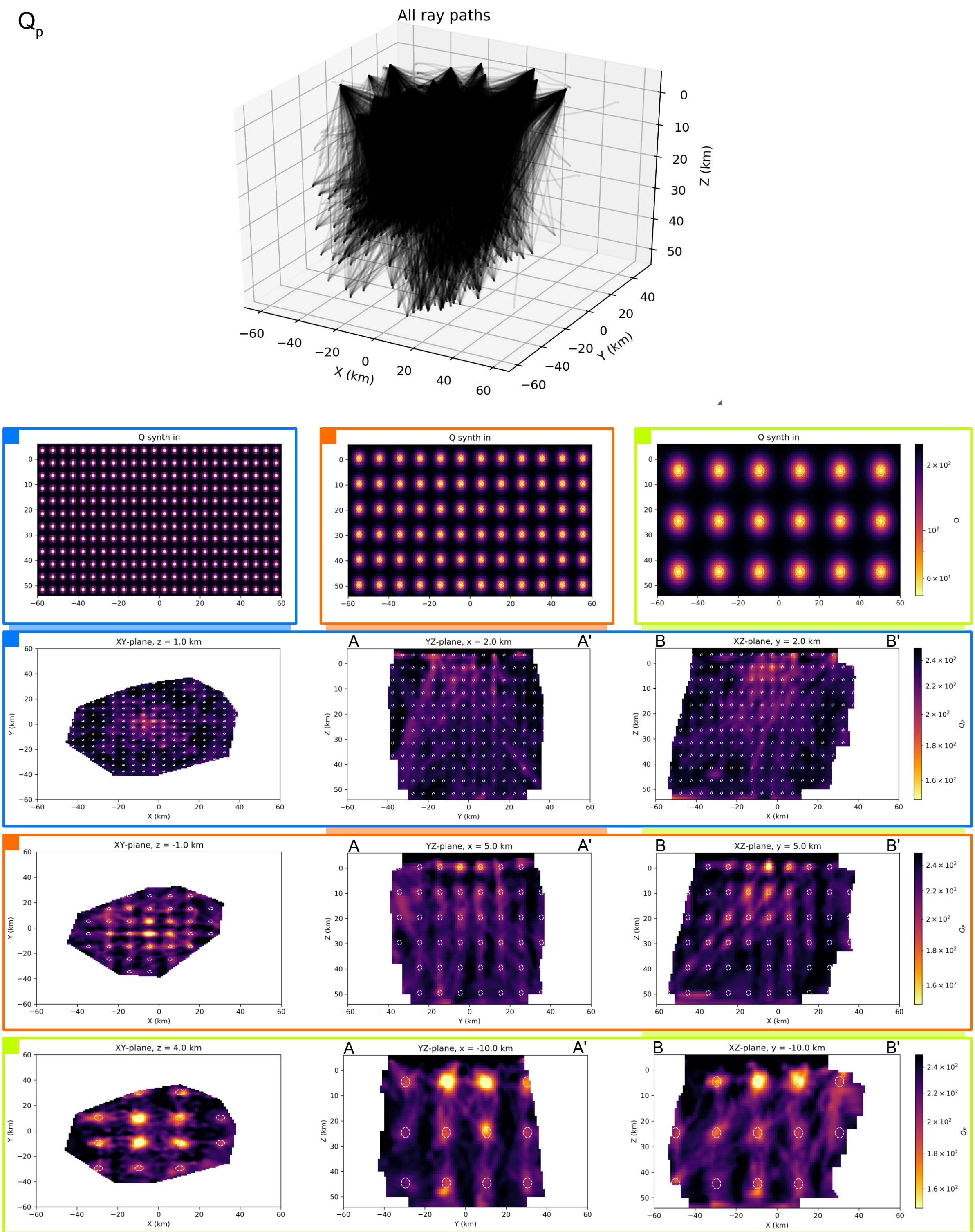

Supplementary Figure 2. Q_P tomography sensitivity analysis. Sensitivity analysis performed based on the theory in Rawlinson & Spakman (2016).

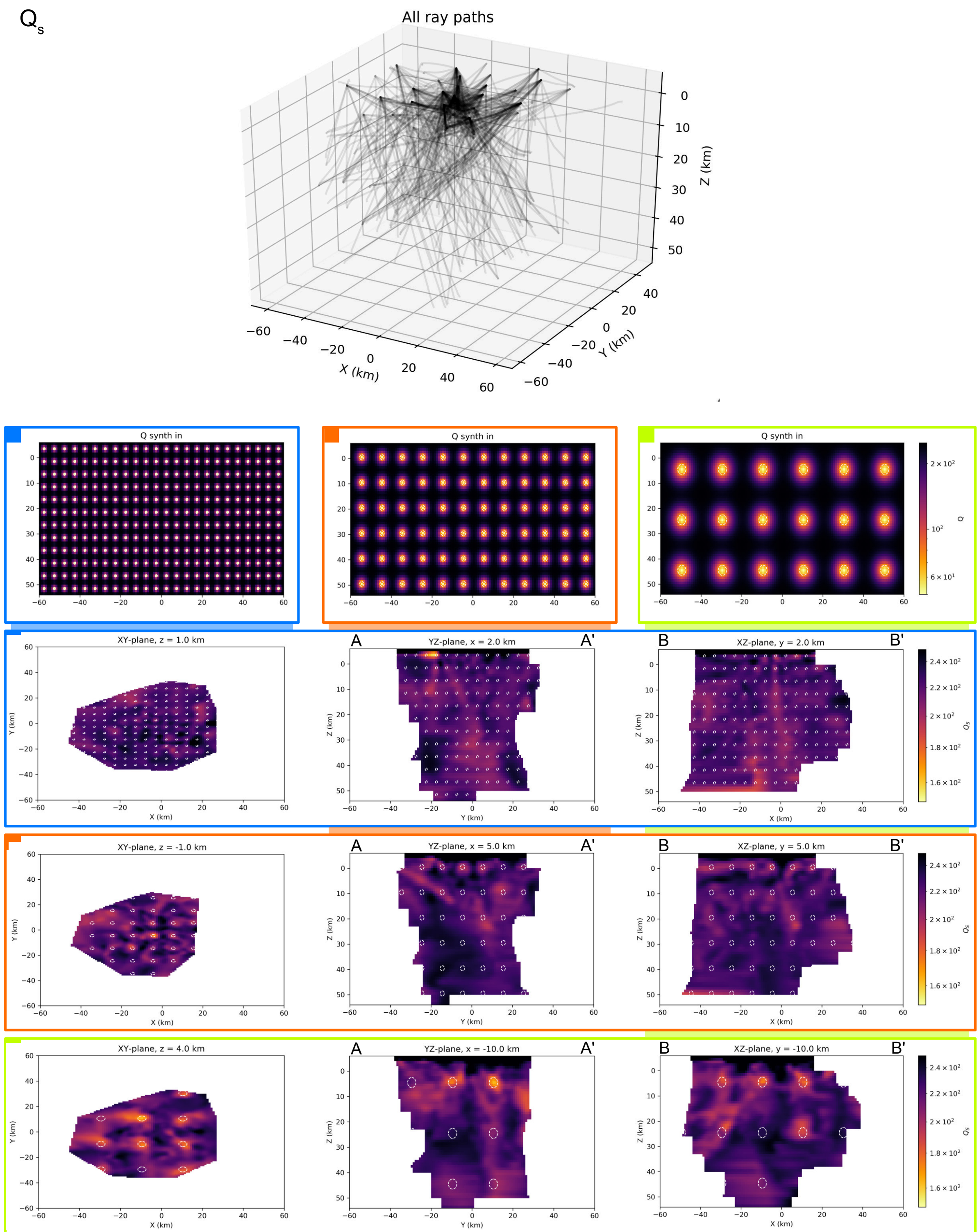

Supplementary Figure 3. Q_S tomography sensitivity analysis. Sensitivity analysis performed based on the theory in Rawlinson & Spakman (2016).

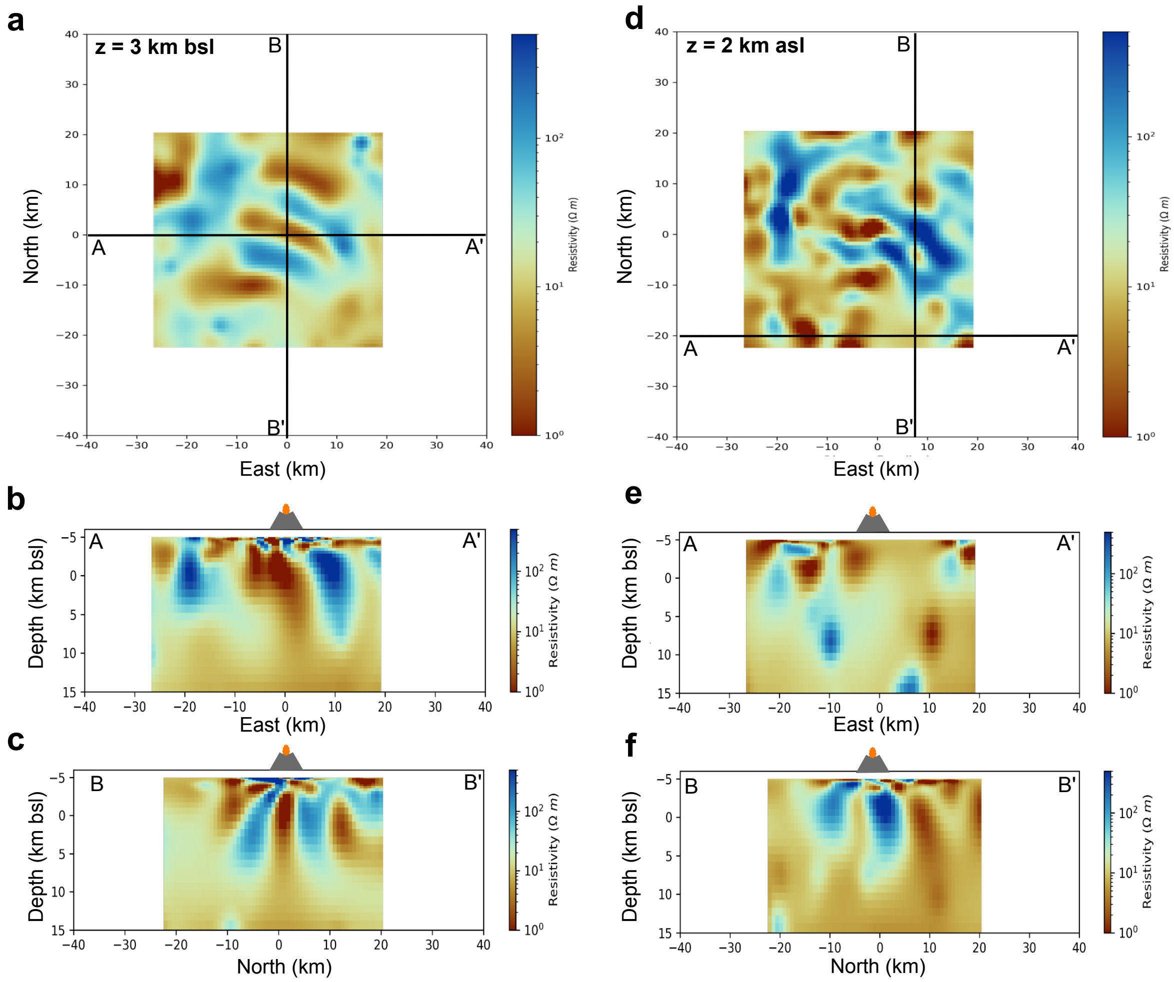

Supplementary Figure 4. Magnetotelluric tomography results from Comeau et al. (2016)**.**

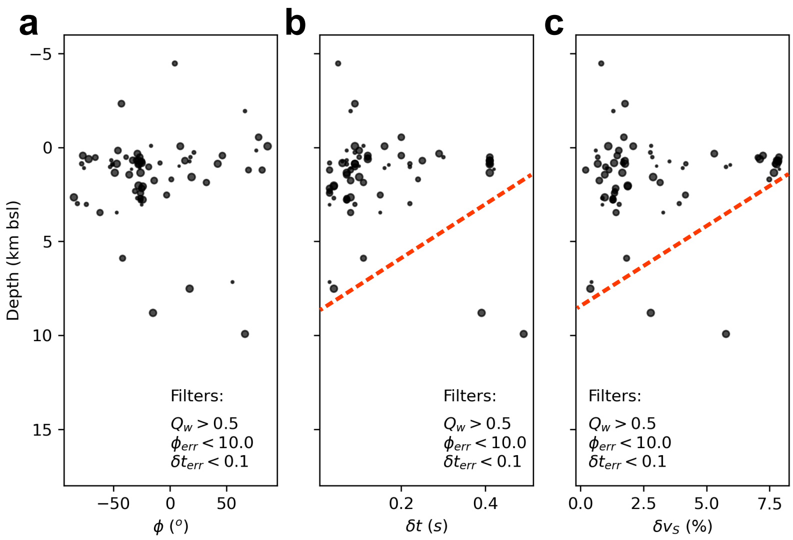

Supplementary Figure 5. Shear-wave velocity anisotropy with depth. (a), (b), (c) Fast directions, delay-times and fractional-change in S-wave velocity with depth, respectively. Relative sizes of scatter points are determined by their associated anisotropic quality factor, Q_W. Red dashed lines in (b), (c) indicate the approximate decreasing trend in delay-time and velocity-change with depth.